

## RESEARCH ARTICLE - APPLICATION

# Effects of nerve bundle geometry on neurotrauma evaluation

Ilaria Cinelli<sup>1</sup>  | Michel Destrade<sup>2</sup>  | Peter McHugh<sup>1</sup>  | Maeve Duffy<sup>3</sup> 

<sup>1</sup>Discipline of Biomedical Engineering, National University of Ireland, Galway, Ireland

<sup>2</sup>School of Mathematics, Statistics and Ap, NUI, Galway, Ireland

<sup>3</sup>Electrical and Electronic Engineering, National University of Ireland, Galway, Ireland

## Correspondence

Ilaria Cinelli, Discipline of Biomedical Engineering, National University of Ireland, Galway, Ireland.  
Email: i.cinelli1@nuigalway.ie; i\_cinelli@yahoo.it

## Funding information

Galway University Foundation; Power Electronics Research Centre; Biomechanics Research Centre

## Abstract

**Objective:** We confirm that alteration of a neuron structure can induce abnormalities in signal propagation for nervous systems, as observed in brain damage. Here, we investigate the effects of geometrical changes and damage of a neuron structure in 2 scaled nerve bundle models, made of myelinated nerve fibers or unmyelinated nerve fibers.

**Methods:** We propose a 3D finite element model of nerve bundles, combining a real-time full electromechanical coupling, a modulated threshold for spiking activation, and independent alteration of the electrical properties for each fiber. We then simulate mechanical compression and tension to induce damage at the membrane of a nerve bundle made of 4 fibers. We examine the resulting changes in strain and neural activity by considering in turn the cases of intact and traumatized nerve membranes.

**Results:** Our results show lower strain and lower electrophysiological impairments in unmyelinated fibers than in myelinated fibers, higher deformation levels in larger bundles, and higher electrophysiological impairments in smaller bundles.

**Conclusion:** We conclude that the insulation sheath of myelin constricts the membrane deformation and scatters plastic strains within the bundle, that larger bundles deform more than small bundles, and that small fibers tolerate a higher level of elongation before mechanical failure.

## KEYWORDS

coupled electromechanical modeling, diffuse axonal injury, electrothermal equivalence, finite element modeling, neurotrauma

## 1 | INTRODUCTION

Head injuries may result in traumatic brain injury (TBI), which is categorized as mild, moderate, and severe based on clinical symptoms and postmortem histology.<sup>1-5</sup> The rapid acceleration-deceleration of the head during TBI generates a diffusive form of microscale damage, such as diffuse axonal injury (DAI) and microvascular damage.<sup>1,3-5</sup> However, microscale damage is difficult to detect with the current medical imaging technology due to hemorrhages, hematomas, and tissue lesions of the neighboring injured area.<sup>1,4,6</sup> This difficulty increases the risk of developing future neurodegenerative disease.<sup>1,6</sup>

Previous biomechanical studies of brain injuries have highlighted the importance of brain microenvironment and of neural tissue responses in the understanding of disease pathogenesis initiated by TBI.<sup>1</sup> They established that tensile axonal strain is the most realistic mechanism for generating DAI at the cellular level.<sup>7-9,4,10</sup>

At the next level, the distribution of diffuse damage is found to be nonuniform throughout the brain tissue, suggesting that tissue regions and cellular structures within the brain are affected differently.<sup>1</sup> Tissue heterogeneity has a significant influence on the mechanotransduction of mechanical forces into physiological and neural responses of nervous cells,<sup>1</sup> and therefore, models that accurately account for tissue structure are needed for an effective modeling of damage.

Experiments have also revealed a close link between changes in electrical signal propagation and changes in the geometrical structure of neurons.<sup>11</sup> Indeed, a geometrical alteration of neural morphology can modify the propagation properties of the action potential, for instance by delaying propagation.<sup>12-14</sup> A detailed investigation of nonrecoverable deformations of the neural microenvironment (injuries,<sup>4,9</sup> trauma,<sup>9</sup> and tumors<sup>14</sup>) is needed to evaluate and estimate the role of nerve bundle geometry in changing neural activity.

Recent progress in physiological measurements has led to new insights into damaged neuronal behavior, where electrophysiological and functional deficits of the neural activity are known to be functions of the applied strain and strain rate.<sup>9,12,15</sup> Electrophysiological impairments (such as leaking ionic channels<sup>12,16</sup>) are associated with structural damage of the neuron tissue. The loss of nerve membrane integrity due to an applied deformation leads to changes in electrical signal propagation.<sup>16,17</sup> Furthermore, injury pathologies in nerve fibers are also initiated and influenced by strain and strain rate, which have a significant impact on the time of neural death and pathomorphology, respectively.<sup>18</sup> For instance, experimental studies on human axons show that morphological changes may tolerate dynamic stretch at strains up to 65 %, <sup>19</sup> manifesting both an elastic recovery and a delayed elastic response along the fiber length.<sup>19</sup>

Here, we evaluate the influence of neuron morphology in neurotrauma, which refers to the alteration of neural activity in a mechanical-injured nerve,<sup>15,17</sup> using a fully coupled electromechanical model in the finite element software package Abaqus. Our purpose is to evaluate strain distributions leading to neurotrauma in damaged nerve bundles of different types and sizes during signaling. This work aims at improving the understanding the mechanotransduction of mechanical loads below the threshold for mechanical failure, on neural responses in nerve bundles and fibers.

In contrast with previous modeling efforts,<sup>9,14</sup> we propose a fully coupled 3D electromechanical model of a nerve bundle,<sup>8,20</sup> which includes electromechanical coupling<sup>11,21,22</sup> of the neural activity. We apply mechanical loads inducing damage<sup>8,9</sup> at the nerve membrane layer to investigate the changes in neuronal membrane excitability<sup>9</sup> and propagation<sup>12</sup> in response to changes in electrostriction.<sup>23</sup> The electrical and the mechanical fields of the model are coupled by using electrothermal equivalences and equivalent materials properties in finite element analysis.<sup>8,20</sup> We achieve coupling of the electromechanical effects of the action potential<sup>24</sup> by modeling the nerve membrane as a piezoelectric material<sup>11</sup> and implementing the thermal analogy of the neural activity.<sup>8,20</sup>

The modeling approach reported in Cinelli et al.<sup>8</sup> describes a computationally efficient way for coupling the electrical and mechanical domains in finite element analysis. It has been shown to replicate successfully complex biophysical phenomena occurring in nervous cells. The nerve bundle model in Cinelli et al.<sup>8</sup> assumes incompressible rate-independent isotropic mechanical behavior,<sup>8,22</sup> so that the applied loads induce elastic deformations only while no permanent deformations are generated within that model. In contrast to Cinelli et al.,<sup>8</sup> here, the description of the mechanical behavior of the nerve bundle model incorporates plasticity to represent permanent deformation of the tissue, while sharing the same approach for modeling the coupling between electrical and mechanical domains, proposed in Cinelli et al.<sup>8</sup> The incorporation of plasticity in this way significantly enhances the physiological accuracy of the model in relation to recoverable (elastic) and permanent (plastic) tissue deformation. This aspect is of critical importance when investigating the effects of trauma, as here. Understanding the role of plasticity on induced alterations of the neural activity might lead to new insights into the mechanical and functional performance of nervous cells.

Although nerve axons show some elastic recovery of the prestretched geometry under slow loading rates,<sup>19</sup> the role of plasticity in delaying the mechanical response is fundamental in understanding the pathology due to stretch injury occurring at fast loading rates. Indeed, induced-permanent focal axonal dysfunction and induced-permanent focal electrophysiological impairments may explain the adaptive recovery of neural connections seen in mild-to-moderate TBI and the potential synaptic rearrangements seen in severe TBI.<sup>25,26,27</sup>

We also show that variability in axonal caliber affects axonal vulnerability, leading to differential injury responses in myelinated and unmyelinated axons.<sup>1,28</sup> Morphological changes of the cellular structures are more likely to happen in unmyelinated than myelinated axons,<sup>1,25,29</sup> and they occur in the form of molecular-based processes such as leaking

nerve membrane<sup>16</sup> and cytoskeleton disruption.<sup>1,19,25,30</sup> Unmyelinated axons are at greater risk compared with myelinated axons, where injuries occur preferentially at the Ranvier node regions.<sup>1</sup> Additionally, larger caliber axons are shown to be more vulnerable to injury due to their higher metabolic requirements, and they are more prone to develop pathologies.<sup>1,29</sup>

Our proposed 3D finite element model of a nerve bundle includes a representation of a nervous cell made of extracellular media, a membrane, and intracellular media (ICM). The bundle model is a section of an idealized geometry of a nerve bundle consisting of 4 identical parallel cylindrical unmyelinated or myelinated fibers (see Figure 1). The diameters of these fibers are within the range of small fibers of the human corpus callosum.<sup>31</sup> We consider the case of 2 scaled nerve bundle models with a ratio of 2:1, where the nerve fibers inside follow the same ratio, keeping the same thickness for the nerve membrane.<sup>8,20</sup> The bundles are made of identical unmyelinated or myelinated nerve fibers. We use different sizes and nerve types to enhance the understanding of neurotrauma in mechanically injured bundles, as revealed in experiments at the cellular level.<sup>15-17</sup>

The use of a 3D geometry with plastic material properties allows for the simulation and evaluation of strain and voltage distributions before and after the induced damage. The inclusion of 3D mechanically induced electrophysiological impairments is needed to enhance the understanding of electromechanical changes in neurotrauma evaluation and improve diagnosis, clinical treatment, and prognosis.<sup>3,32</sup> This approach might prove crucial to study and understand the mechanics at play in neurophysiology, as observed experimentally in damaged nerve membranes of clinical cases such as multiple sclerosis.<sup>15,17,33</sup>

## 2 | METHODS

### 2.1 | Model

With the purpose of highlighting the importance of a unified electromechanical theory for neural applications,<sup>1,22,23,34,35</sup> a modeling approach<sup>8,20</sup> is further tested in this paper to improve the accuracy in replicating complex electromechanical phenomena accompanying the neural electrical activity.<sup>8,20,22,23</sup>

This work is based on an established electromechanical coupling,<sup>8</sup> previously verified and validated in the finite element software Abaqus CAE 6.13-3.<sup>8,20</sup> This coupling is a modeling approach where equivalent thermal properties are used for representing electrical quantities.<sup>8,20</sup> Therefore, here, the temperature is representative of voltage.<sup>20</sup> The coupling was verified on animal models<sup>20</sup> and nerve bundle models within the range of small fibers of the human corpus callosum.<sup>8</sup> Published experimental evidence for axons under mechanical loading show the importance of plasticity in understanding phenomena such as recovery or disease.<sup>19,25,26,27</sup> In this paper, we have assumed that the nerve membrane, ICM, and myelin regions are characterized by similar plastic isotropic behavior,<sup>7,9,19,22</sup> as discussed in section 2.2. The plastic behavior is calibrated in Abaqus CAE. Then, the coupling utilizes the total strain (elastic, plastic, and thermal [piezoelectric] strain) to modify the electrical activity of a nerve bundle model, as discussed in section 2.3. In this

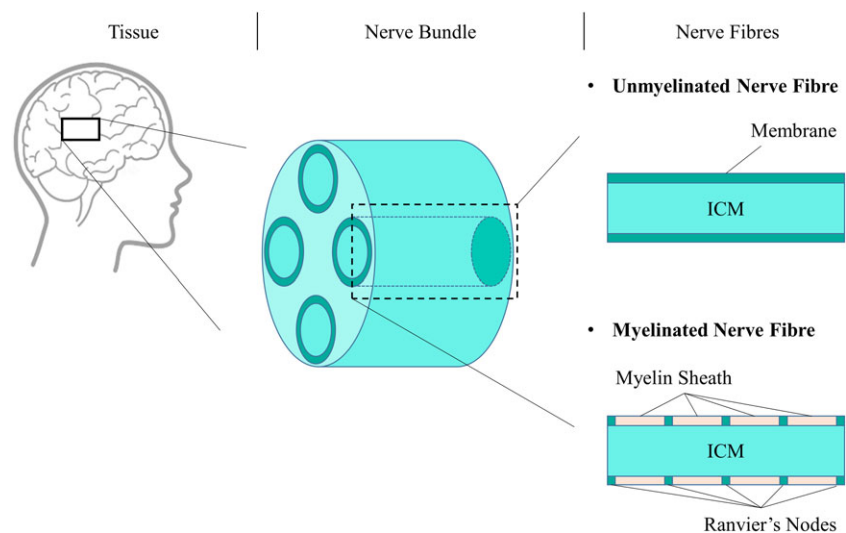


**FIGURE 1** Sketch of the nerve bundle geometry. The bundle is made of 4 identical fibers (ECM, extracellular media; ICM, intracellular media)

paper, the use of an idealized geometry of a nerve bundle is meant to reduce complexity and computational cost arising from the use of 3D morphological images of neuronal structure.<sup>8,36</sup>

Our bundle model simulates the exchange of charges in 4 identical cylindrical neurites, made of an ICM enclosed by a thin membrane, and surrounded by extracellular media<sup>8,20</sup> as shown in Cinelli et al.<sup>8</sup> Additionally, 2 fiber bundle models are considered, scaled in size in the ratio of 2:1. Here, only the cases of a fully unmyelinated bundle or a fully myelinated bundle are considered, but the same process may be applied to investigate mixed fiber bundles.

Regardless of the diameter, the nerve membrane layer has a finite thickness equal to 3 nm, representing the dielectric part of the membrane only.<sup>20,37</sup> Instead, the myelin layer of myelinated fiber is a periodically partitioned region at the nerve membrane layer, with the same finite thickness<sup>8,38</sup> (see Figure 1). The reason for this assumption is motivated by the use of the cable equation for simulating diffusion of charges in heterogeneous conductors as discussed by Einziger et al.<sup>38</sup> Thus, the cable equation models charge diffusion in homogeneous and heterogeneous conductors (ie, unmyelinated and myelinated fibers, respectively), and this can be implemented as an equivalent thermal process in finite element analysis.<sup>8,20</sup>

## 2.2 | Material properties

We assume incompressible isotropic mechanical properties.<sup>22</sup> We also assume the same isotropic plastic behavior for the nerve membrane, ICM, and myelin layer. The yield stress is calculated with an engineering strain equal to 21 %<sup>7</sup> and a Young modulus equal to 1GPa.<sup>22</sup> Strain hardening is assumed to occur up to a strain of 65 %.<sup>19</sup> Thus, the engineering strain and engineering stress values are (0.21, 0.21 GPa) and (0.65, 0.65 GPa) for the yield strain limit and strain hardening, respectively. Beyond 65 % strain, the stresses are assumed to remain constant.

The electrical model parameters for unmyelinated and myelinated fibers are taken from Cinelli et al and Jérusalem et al,<sup>8,9</sup> respectively. This model assumes that the exchange of charges occurs in the through-thickness direction of the nerve membrane, rather than along the fiber length.<sup>8,11,24</sup> So, the piezoelectric effect is only relevant in the through-thickness direction, represented here with orthotropic piezoelectric constants of approximately 1 nm per 100 mV<sup>11</sup> in the thickness direction and zero in the longitudinal and circumferential directions, while the electrical capacitance per unit area,  $C_m$ , changes as the square of the voltage.<sup>8,21,22</sup>

## 2.3 | Implementation

We expand on the Hodgkin and Huxley (HH) model to include 3D fields, elasticity, and plasticity (see contrast depicted in Figure 2). With the electrothermal equivalences,<sup>8,20</sup> we can visualize in 3D the neural activity, the distribution of voltage, and the generated strain, using well-established coupled thermomechanical software simulation tools.<sup>8,20</sup> This model is implemented as a coupled thermomechanical model in the finite element software code Abaqus CAE 6.13-3, where electricity is simulated as thermal analogy.<sup>20</sup>

Then, by using user-defined subroutines,<sup>8,20</sup> thermal equivalent electrical properties are assigned to the membrane of each fiber in the bundle, independently, based on the spike initiation,<sup>39</sup> strain,<sup>9,12</sup> and voltage<sup>21</sup> generated at each membrane. As in Cinelli et al,<sup>8</sup> the membrane neural activity changes in response to the membrane voltage  $V$ , total strain,  $\epsilon$ , at the membrane,<sup>9,24</sup> space, and time. In contrast to Cinelli et al,<sup>8</sup> here, total strain includes elastic, piezoelectric (thermal equivalent<sup>20</sup>), and plastic strain (see Figure 2).

The HH reversal voltage potentials of sodium,  $E_{Na}$ , and potassium,  $E_K$ , change due to voltage and strain at the nerve membrane,<sup>9,12</sup> and hence, the threshold of action potential initiation changes.<sup>24</sup> In particular, the axial component of the total strain, read along the fiber length, links mechanical loads and electrical activity in nervous cells<sup>8,9</sup> inducing changes in reversal potentials at the nerve membrane, as discussed by Jérusalem et al.<sup>9</sup> Then, the reversal potential of the leak ions  $E_{l^-}$  is not influenced by the strain but varies based on changes in the gradient concentrations of potassium and sodium across the membrane.<sup>9</sup>

For traumatized channels, the changes in conductivity for sodium,  $G_{Na}$ , and potassium ions,  $G_K$ , follow the changes in the respective reversal potentials.<sup>24</sup> Additionally, the nerve membrane integrity varies with the fraction of nodal channels (AC) affected by the trauma, while the other membrane's channels,  $(1 - AC)$ , remain intact<sup>12</sup> (see Cinelli et al<sup>8,20</sup>). Here, only the extreme cases of the entire membrane being traumatized ( $AC = 1$ ) or intact ( $AC = 0$ ) are shown as illustrative examples.

## 2.4 | Boundary conditions

For evaluating the influence of neuron structure in neurotrauma, we assume only 1 active fiber in each bundle, Fiber #3, while the other fibers are activated by the diffusion of charges when the induced damage is minimal or absent.<sup>8</sup> For the purposes of this paper, the 1-fiber activation assumption allows for quantifying the generated electromechanical alterations<sup>8</sup> in a simplified context, as first step toward a more detailed analysis. This assumption allows for understanding the distribution of charges when mechanical damage is induced, focusing on the radial distribution of charges rather than on longitudinal.

In particular, an upper-threshold stimulation voltage with a Gaussian distribution<sup>8,40</sup> is applied on Fiber #3 along its length (see Figure 2), while the other fibers are activated only if the diffused charges from Fiber #3 generate an input voltage higher than the modulated threshold.<sup>39</sup> The 3D distribution of charges on Fiber #3 modulates the activation of the other fibers.<sup>8</sup> When a mechanical load is applied, the imposed deformation (in tension or compression) contributes to the modulation of the activation of the neighboring fibers following the distribution of the applied strain within the bundle.<sup>8</sup>

We consider in turn 2 cases of applied mechanical loads at the bundle. As a first step to assess the inclusion of plasticity by using this novel coupling method, only frequency-independent loading conditions are considered throughout, following the initial steady-state regime (lasting about 2 ms).<sup>8,20</sup> The mechanical loads are applied from 2 to 67 ms, as instantaneous loading conditions, and the model runs for 140 ms so that the effects of plasticity can be observed post loading. An fixed boundary condition is enforced at the origin of each model, so that no movement and rotation is allowed at the origin node. Then, no rotation is allowed for all the nodes at the origin bundle side.

In the first case, we apply an instantaneous uniform compression to the bundle to simulate injury conditions, with 2 values of pressure, simulating mild (less than 55 kPa) and severe (higher than 95 kPa) pressures.<sup>2</sup>

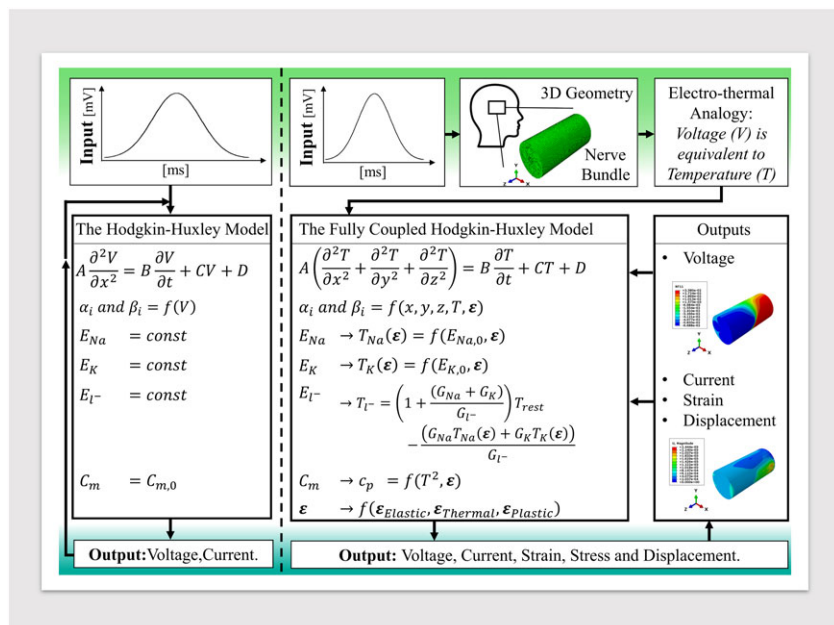
In the second case, we reproduce the axial strain conditions of the uniaxial test conducted by Bain and Meaney.<sup>7</sup> Two values of instantaneous uniform stretch are applied as a displacement boundary condition to simulate 5 % and 14 % of total axial deformation,  $\epsilon$ , where the probability of inducing morphological injury during the elongation test is 5 % and 25 %, respectively.<sup>7</sup> Additionally, we also consider the cases of 25 %, 30 %, and 60 % elongation to investigate the electromechanical responses within the range of plasticity (before mechanical failure).<sup>19</sup>

## 3 | RESULTS

### 3.1 | Pressure loads

Figure 3A shows the membrane potential of a small bundle made of unmyelinated nerve fibers (SBUN), and Figure 3C to E shows the radial displacement in small (SBUN) and big (BBUN) unmyelinated bundles under mild (25 kPa) and

**FIGURE 2** Flowchart of the code describing the active behavior of the nerve's membrane: (left) the uncoupled Hodgkin and Huxley (HH) dynamics<sup>24</sup> and (right) the fully coupled HH dynamics used in this paper. A Gaussian voltage distribution elicits the action potential in a 3D model of a nervous bundle. By electrothermal equivalence, the full HH model is implemented as an equivalent thermal process, with changes in the membrane's conductivity,<sup>24</sup> the capacitance,<sup>20</sup> and the HH parameters<sup>9</sup>



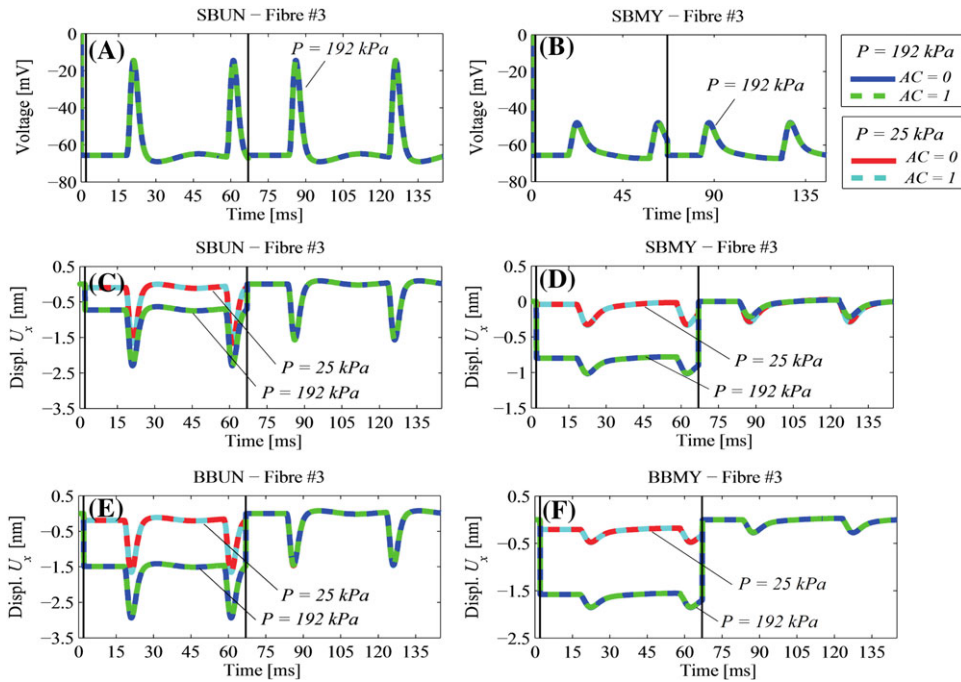


**FIGURE 3** (A) Membrane potential [mV] on Fiber #3 in a small unmyelinated bundle. (B) Membrane potential [mV] on Fiber #3 in a small myelinated bundle. Radial displacement [nm],  $U_x$ , of unmyelinated small (C) and big (E) bundles and myelinated small (D) and big (F) bundles. The uniform applied loads are classified as mild (25 kPa) and severe (192 kPa) pressures.<sup>2</sup> Data are the maximum radial displacement of a node on Fiber #3 in both cases

severe (192 kPa) pressures inducing axonal injuries.<sup>2</sup> Figure 3B shows the membrane potential of a small myelinated bundle (SBMY). Figure 3D to F shows the radial displacement in small (SBMY) and big (BBMY) myelinated bundles for each pressure case. Note that we find the same voltage responses for both small and big bundle models because they have the same membrane properties. Here, the strain applied at the nerve membrane by compressing the bundle shifts the ionic reversal potentials of the fully coupled HH model by a quantity which varies depending on the magnitude of the applied load (see flowchart in Figure 2). Results are taken at the maximum radial displacement on Fiber #3.

We find that mild (25 kPa) and severe (192 kPa) pressure levels have a similar impact on the signal transmission, both in reduced magnitude and shift over time, due to similar strain values read at the nerve membrane. In both small (SBUN) and big (BBUN) unmyelinated bundles, the action potential peak is  $-14.4$  mV at 19 ms (see Figure 3A), while in small (SBMY) and big (BBMY) myelinated bundles, the peak is  $-47.54$  mV at 22 ms (see Figure 3B).

For any applied load, the reversal voltage potentials are changed due to the induced strain in the bundle and the magnitude of the action potential is reduced.<sup>9</sup> The applied compression leads to changes in reversal potentials, according to the strain values read along the bundle middle axis only.<sup>9</sup> In all cases, only slight differences are found for a traumatized ( $AC = 1$ ) compared with a nontraumatized nerve membrane ( $AC = 0$ ) when mild or severe pressures are applied, see Figure 3A and B. The AC variable impacts the ionic conductance<sup>12</sup> whose changes are not contributing to the total strain along the bundle middle axis direction during compression. This is because we modeled the piezoelectricity of the membrane radially rather than longitudinally,<sup>8,11</sup> as discussed in Zhang et al, El Hady and Machta, and Hodgkin and Huxley.<sup>11,22,24</sup> Indeed, the applied pressures lead to an axial displacement of less than 1 % of the total length of the bundles in each model. Despite the size of the bundle, traumatized nerve membranes seem to be able to carry and generate signals both during and after uniform compression.

Figure 3C and E shows the radial displacement on Fiber #3 in SBUN and BBUN, respectively. While the shift in baseline displacement is proportional to the applied pressure in both cases, the amplitude of the peak value from the baseline follows the membrane voltage response, and therefore, values for the unmyelinated bundles are the same regardless of the bundle size (see Figure 3C and E).

In Table 1, we collected the values of the displacement shift, during and after loading, at mild (25 kPa) and severe (192 kPa) pressure levels. We also computed the maximum values of the plastic strain (PE) and total strain ( $E_{\text{tot}}$ ) once the loads are removed.

**TABLE 1** Displacements and strains on fiber #3 when compression is applied

Boundary Conditions	Intensity	Unmyelinated Nerve Bundles		Myelinated Nerve Bundles	
		SBUN	BBUN	SBMY	BBMY
Displacement Peak [nm]					
During loading	25 kPa	-1.67	-1.65	-0.34	-0.48
	192 kPa	-2.30	-2.95	-1.02	-1.85
After loading	25 kPa	-1.47	-1.47	0	0
	192 kPa	-1.47	-1.47	-0.28	-0.26
Strain [%]					
Plastic strain	25 kPa	0.5	0.5	0	0
	192 kPa				
Max. total strain	25 kPa	3.5	3.5	1.5	1.5
	192 kPa				

Figure 4A to D shows the difference in voltage distribution over the bundle, at the action potential peak, in small and big, myelinated, and unmyelinated bundles, with nontraumatized nerve membranes ( $AC = 0$ ) bundles, under mild pressure (25 kPa).

The myelinated bundles (Figure 4A and C) experience uniform compression. At the peak of the membrane potential applied on Fiber #3, the piezoelectric effect generates an additional contraction on its nerve membrane, dragging parts of Fibers #2 and #4 in its vicinity. Thus, we find 4 peaks of the maximum total strain  $E_{tot}$  on Fiber #3: 2 are at the regions in proximity to Fibers #2 and #4 and 2 in the diametrically opposed regions (to conserve the overall volume by incompressibility). Then, on the fixed side of the bundle, where the applied voltage is higher, local regions of high voltage are found on Fibers #2 and #4, due to their vicinity with Fiber #3. So, local contractions on Fibers #2 and #4 act in opposition to the contractions on Fiber #3. The voltage distribution in Figure 4A and C is influenced by the final distribution of  $E_{tot}$ . Hence, the voltage is higher at the regions where the applied voltage Gaussian distribution is high, the nerve membrane is not constrained, and the strains are low.

A similar scenario occurs for myelinated bundles (see Figure 4B and D). However, here the piezoelectricity is limited to the Ranvier node regions, whose displacement is constrained by the myelin layer. Accordingly, the  $E_{tot}$  is more

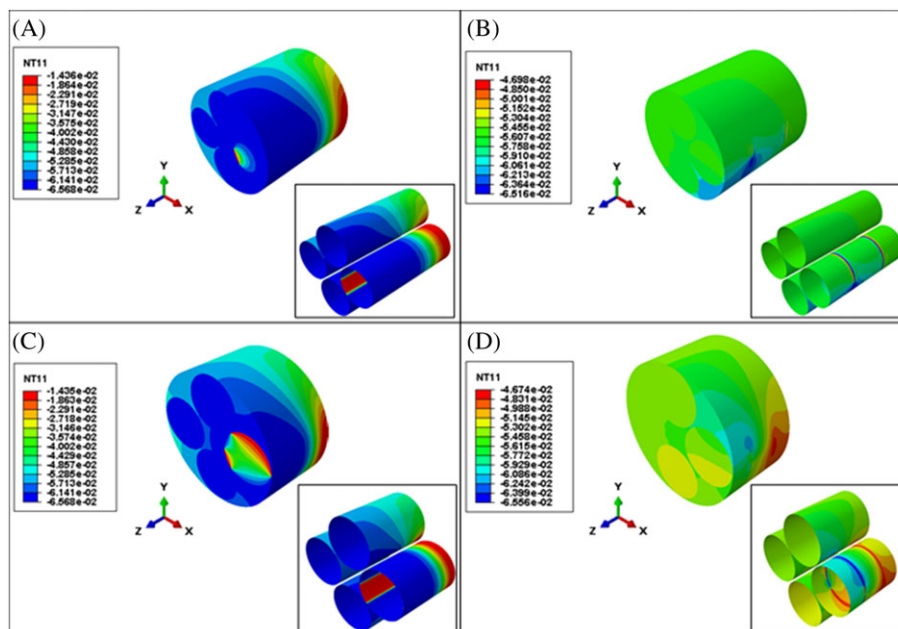


**FIGURE 4** Voltage distribution (NT11), at the action potential peak, in small (A) and big (C) unmyelinated bundles and small (B) and big (D) myelinated bundles for 25 kPa pressure with  $AC = 0$  (intact membranes). The small box shows the membrane layer of each model. These bundles are fully myelinated or fully unmyelinated

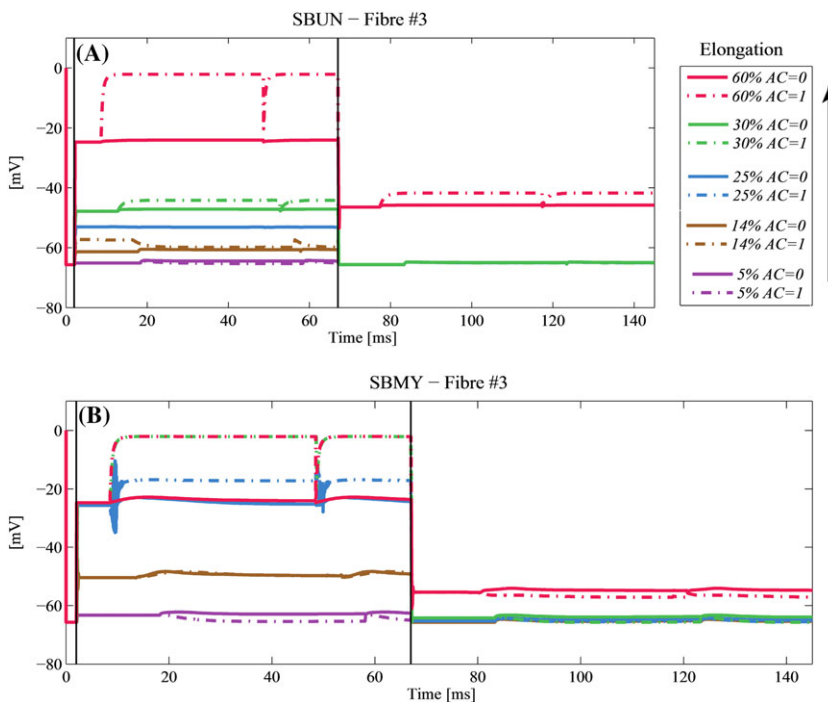
uniform at the nerve membrane layer of all the fibers than for unmyelinated bundles. Fibers surrounding the active Fiber #3 are not activated because the charge read at their nerve membrane is lower than the minimum threshold for activation.<sup>24</sup>

### 3.2 | Displacement loads

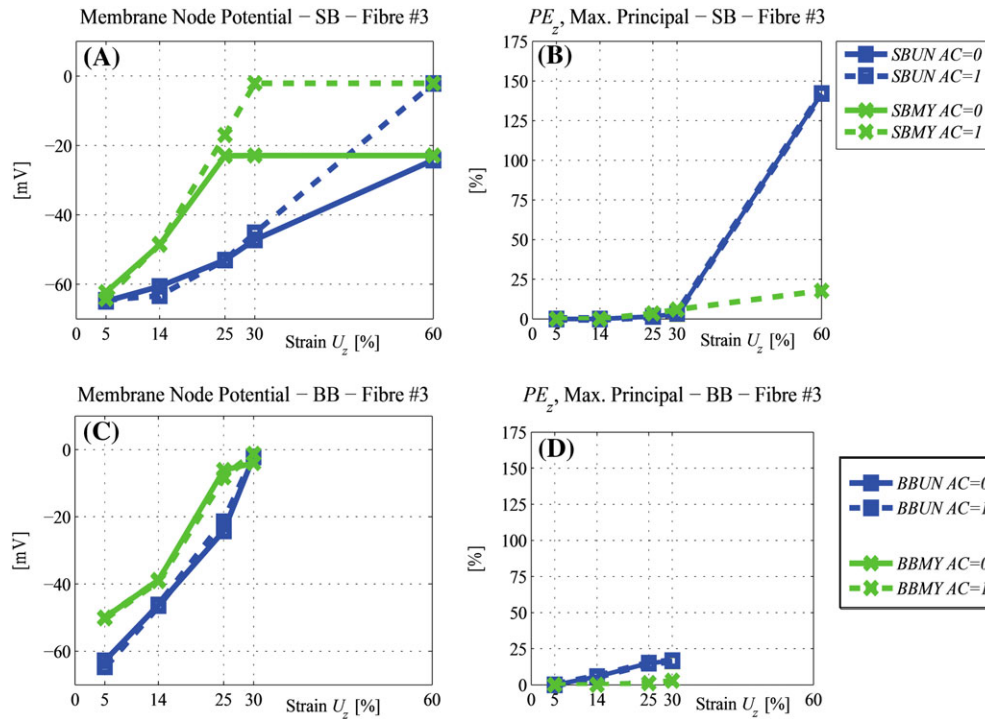
Figures 5–8 illustrate the response of a bundle to a displacement boundary condition applied at one end along its fiber length, simulating 5 %, 14 %, 25 %, 30 %, and 60 % elongation of the total length of the bundle (in line with the experiments conducted by Bain and Meaney<sup>7</sup>). Those elongation values are chosen to initiate an elastic response if the applied strain is lower than 21 %, <sup>7</sup> or a plastic response if it is higher (according to the experiments conducted by Smith et al<sup>19</sup> on cultured axons). The figures show the membrane potential at the position of maximum displacement on Fiber #3, the maximum principal value of plastic strains ( $PE_z$ ) along the bundle middle axis,<sup>9</sup> and the total strain  $E_{tot}$ .

Figure 5 shows the membrane voltage distribution in small (A) unmyelinated (SBUN) and (B) myelinated bundles (SBMY). In all elongations, we find that the action potential signal is reduced significantly if not eliminated altogether, while there is a clear increasing shift in baseline voltage with increasing applied displacement. The effect of strain on the baseline shift is higher for the myelinated than for the unmyelinated bundles. This finding is in line with previous results, where the voltage read at the nerve membrane varies linearly with the elastic component of the total strain up to 21 %<sup>7</sup> when permanent electrophysiological impairments (such as leaking ionic channels<sup>12,16</sup>) alter the osmotic gradient across the membrane, and so the ability to carry and generate action potentials.<sup>9,17,19</sup> Then, the reversal potentials change depending on the level of elongation, the type of bundle, and its size, due to the different distribution of total strain within the bundle.

Additionally, the fraction of nodal channels affected by trauma AC induces differences in the membrane voltage peaks from the membrane baseline (see Figure 5A and B), while there are little or no differences membrane baseline value with varying AC. In the SBUN case, increasing the fraction AC increases the difference between the membrane potential peak and the membrane baseline at higher strains only in small unmyelinated bundles. For example, at 60 %, the membrane potential is  $-24.15$  mV with  $AC = 0$  and  $-2.134$  mV with  $AC = 1$  (see Figure 5A). In SBMY, instead, the membrane peaks at 25 % are about the same as the values found at 30 and 60 % of elongation (see Figure 5B). Similarly to SBUN, the maximum voltage in SBMY at 60 % elongation is  $-23.21$  mV with  $AC = 0$  and  $-2.08$  mV with  $AC = 1$  (see Figure 5B). Then, at high applied strain, the voltage peaks in big unmyelinated bundles (BBUN) show similar differences when going from  $AC = 0$  to  $AC = 1$  ( $-24.17$  mV with  $AC = 0$  and  $-2.15$  mV with  $AC = 1$ , not shown here), while in big unmyelinated bundles (BBMY), the peaks are about the same order regardless of



**FIGURE 5** Membrane potential [mV] on Fiber #3 in small (A) unmyelinated and (B) myelinated bundles, under 5 % to 60 % elongation. The load is applied from time  $t = 2$  ms to time  $t = 67$  ms. The fraction of ionic channels affected by the strain is  $AC = 0$  for an intact membrane and  $AC = 1$  for a traumatized membrane.<sup>12</sup> Data are taken at the maximum displacement along the bundle middle axis on Fiber #3



**FIGURE 6** Peak values of the membrane potential [mV] in (A) small and (C) big bundles and maximum values of the maximum principal plastic strain at the node of interest, along the bundle axis, for (B) small and (D) big bundles. Data are taken on fiber #3 at the node where the displacement along the bundle axis is maximum. The axial elongations are 5 %, 14 %, 25 %, 30 % and 60 %. In big bundles, failure occurs at 30 % applied displacement

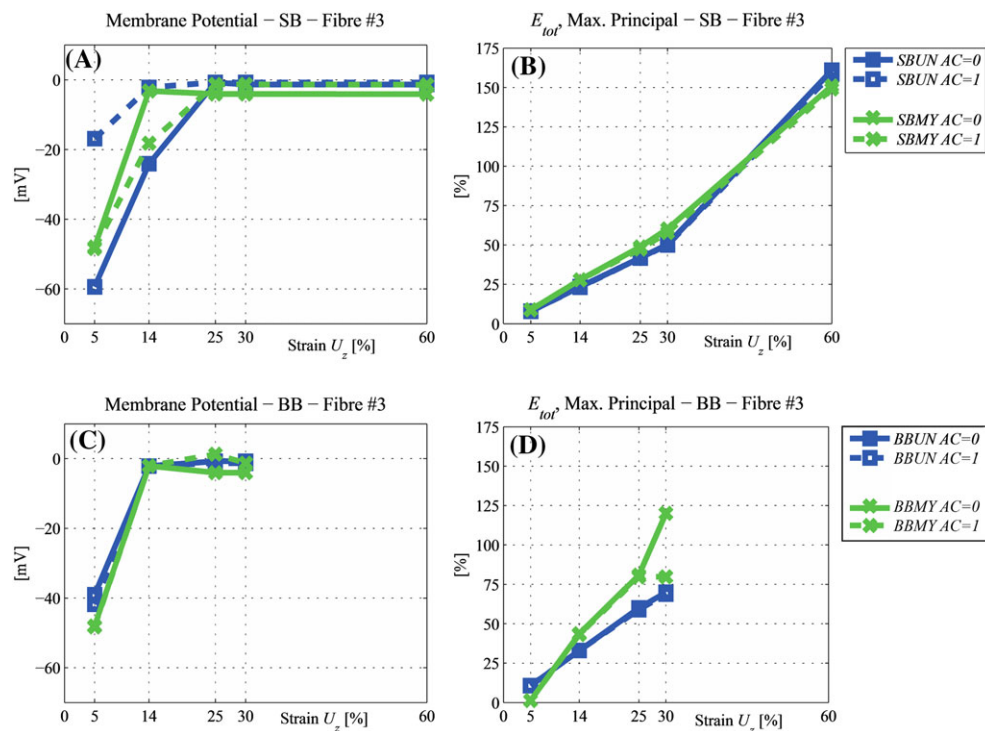


**FIGURE 7** (A and C) The peak values of the membrane potential [mV] found on fiber #3, in the SB and BB, respectively. (B and D) The maximum value of the total strain ( $E_{tot}$ ) is the maximum found on fiber #3. Data are taken at the maximum peak voltage in all the cases. Strains are 5 %, 14 %, 25 %, 30 % and 60 %. In BB, failure occurs at 30 % applied displacement

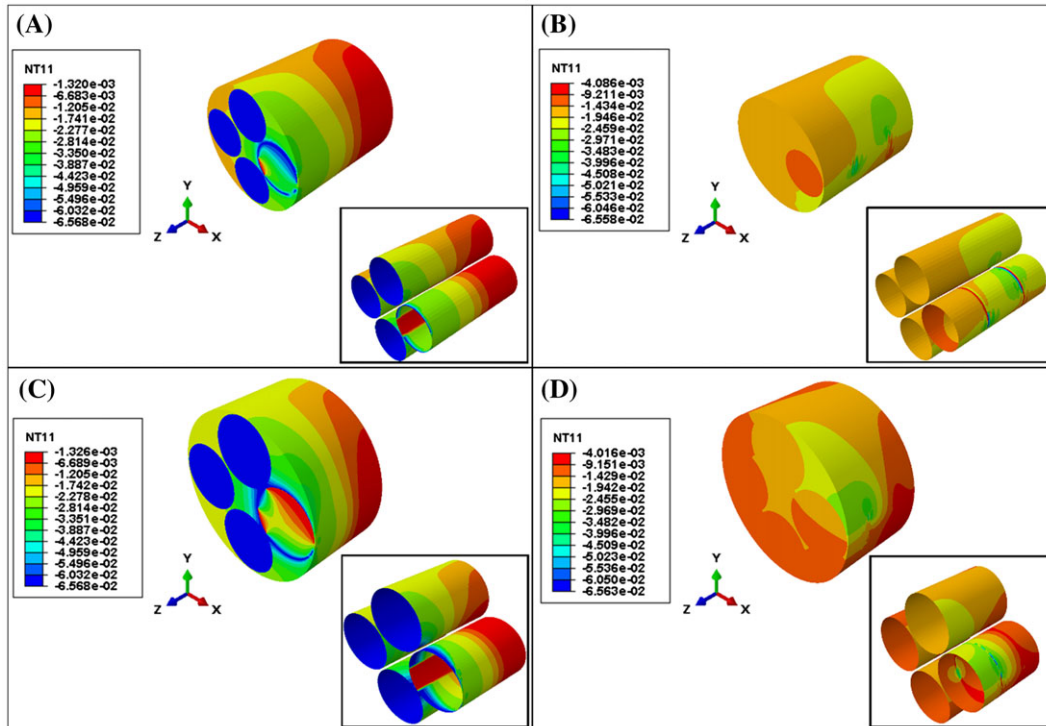


**FIGURE 8** Isometric view of (A) SBUN and (B) SBMY for 60 % elongation and (C) BBUN and (D) BBMY for 30 % elongation with  $AC = 0$ . Data are taken at the peak of the action potential. NT11 is the equivalent voltage variable [in V]. The box shows the membrane layer of each model. These bundles are fully myelinated or fully unmyelinated

AC ( $-4$  mV with  $AC = 0$  and  $-1$  mV with  $AC = 1$ , not shown here). However, big bundles show higher shift in membrane potential at 30 % elongation, which is the maximum elongation for big bundles in this study.

These trends are to be expected because the fraction of nodal channels affected by trauma  $AC$  impacts the ionic conductance of the nerve membrane.<sup>12</sup> Hence, with  $AC = 1$ , a membrane plateau is reached because of the combined changes in ionic conductance<sup>12</sup> and in reversal potentials.<sup>9</sup> The plateau shape occurs due to the similar values of the reversal potentials in a membrane in which the ion mobility of potassium and sodium are similar.

In unmyelinated fibers, the membrane voltage is shifted following elongation and no action potential is generated because of the higher strain components along the fiber length, where the strain is highest.<sup>9</sup> In contrast, similarly to compression, the myelin layer induces a different distribution of strain at the Ranvier node regions of the nerve membrane layer, where strains along the bundle middle axis are lower than in unmyelinated bundles, as observed in experiments.<sup>1,25,29</sup> Therefore, those fibers are more likely to generate an action potential after elongation. This is the reason why in SBMY, the potential does not have a plateau shape when  $AC = 1$  as in myelinated fibers (see Figure 5). Then, in the BBMY, the fiber is still able to generate action potential, both during and after loading, although there is a shift in membrane voltage baseline, as seen in the other cases. This suggests that the myelin layer induces a different distribution of strain within the fiber to preserve its functionality.

After the load is removed (ie, after 67 ms), only in the case of 60 % elongation is the membrane baseline for SBUN shifted, up to  $-45.7$  mV ( $AC = 0$ ) and to  $-41.7$  mV ( $AC = 1$ ), as the ionic gate channels are kept open by the permanent plastic strains at the nerve membrane. Similarly for SBMY after loading, the membrane voltage baseline goes to  $-55.64$  mV only for 60 % elongation ( $AC = 0$  and  $AC = 1$ ), while it remains about  $-65$  mV for the other elongation values (see Figure 5). As seen by Jérusalem et al.,<sup>9</sup> we find here that the larger the elongation, the greater the shift of the membrane potential to a higher peak value, where the reversal potentials are affected differently by the strain magnitude.

This effect can be better appreciated in Figures 6 and 7, where membrane voltage peaks and corresponding strains are taken at the node of maximum axial displacement and the node of maximum peak voltage on Fiber #3, respectively. Figure 6 shows the peak of the membrane potential in (a) small and (c) big bundles, and the corresponding plastic strains, (b) and (d), during elongation, at the node of maximum axial displacement along the bundle middle axis (ie, along the  $z$  - axis). The membrane potential (see Figure 6A-C) shows only slight changes with the fraction of nodal

channels affected by trauma AC for strains lower than 30 %. Although the voltage in SBMY levels off at lower strains than in SBUN, at 60 %, the differences in membrane potential are not dependent on fiber type, but only on AC (see Figure 6A). In SBUN and SBMY, the same value of maximum potential is reached at 60 %, which is about  $-20$  mV with  $AC = 0$  and about  $0$  mV with  $AC = 1$  (see Figure 6A). The corresponding PEs are lower than 25 % for applied elongation values lower than 30 %, while they are much higher in SBUN (143 %) than in SBMY (20 %) at 60 % elongation (see Figure 6B). However, the local maximum peak voltage, relative to Fiber #3, reaches a constant value above 25 % elongation (see Figure 7A). Differences in maximum at lower elongations (see Figure 8A) are due to elastic and thermal strains (ie, the thermal equivalent of piezoelectric strain<sup>8</sup>; see Figure 7B) because of the small plastic strains found for the same conditions (see Figure 6B).

In contrast, when doubling the size of the bundles, the changes in membrane potential are of the same order of magnitude for unmyelinated and myelinated bundles in all elongation cases. Additionally, in contrast to what happens to small bundles, AC has a little influence on these voltage variations (see Figure 6C).

Similarly, the local maximum peak voltage read on Fiber #3 does not show great variation with either fiber type or AC during elongation tests (see Figure 7A). Again, slight differences in plastic strains (PE) are found going from  $AC = 0$  to  $AC = 1$  (see Figure 6B and D), suggesting that the changes in ionic conductance<sup>12</sup> have a smaller impact, compared with the applied strain, in generating plastic strain at the nerve membrane. At high strain (here, at 30 %), the peaks, read in both bundles, reach the same value, independent of the fiber type and AC value (see Figure 6C). Although there is a large shift in potential, the plastic strains are lower than 25 % in both BBUN and BBMY. At the same applied strains, the plastic strain is not the main component of the maximum value of the total strain  $E_{tot}$  read at the bundles (see Figure 7D), which are up to 75 % in BBUN and 120 % in BBMY.

Data show that plastic strains are responsible for the functional and mechanical failure in small unmyelinated bundles (SBUN), while functional recovery is more likely to happen in SBMY because the elastic component is 70 % of the  $E_{tot}$  at 60 % elongation (see Figure 7B). Then, larger bundles show higher variation in membrane voltage due to the higher number of changes exchanged per unit area on the fiber. However, the  $E_{tot}$  at 30 % elongation are comparable with the values found in small bundles at 60 %, despite the lower plastic strains (PE) at the membrane. Failure occurs for elongation higher than 30 %, suggesting that the  $E_{tot}$  are mainly along the bundle middle axis. Strains along the fiber length are those with greater impact on the membrane voltage<sup>9</sup> and are responsible for the voltage shift in all the bundles considered here.

Then, myelinated bundles (both SBMY and BBMY) show smaller PE in contrast with unmyelinated bundles (both SBUN and BBUN) at the same elongation. Particularly, at 30 % elongation, the plastic strain is less than 10 % in myelinated bundles (5.90 % in SBMY and 2.88 % in BBMY) and greater than 15 % in unmyelinated bundles (15.42 % in SBUN and 16.56 % in BBUN). The myelin layer seems to redistribute the induced permanent damage on the whole fiber, rather than on the fiber length, as in unmyelinated bundles. Thus, at the same loading conditions, myelinated fibers and bundles are stronger than the unmyelinated ones.

Figure 8A to D shows the difference in total displacement distribution, at the action potential's peak for 30 % elongation and no traumatized nodal channels ( $AC = 0$ ). Similarly to Figure 4, the voltage distribution is affected by the total generated strain  $E_{tot}$  at the nerve membrane layer of each fiber. Here, the fibers are pulled along the bundle middle axis, while Fiber #3 is contracting, dragging Fibers #2 and #4. The maximum value of the total strain  $E_{tot}$  is lower around the center of the bundle due to the balance of negative radial and positive axial strains. Here, the plastic strains (PE) are consistently higher than those generated by applied pressure (see Figure 3). Again, the voltage is higher in the regions where lower strains are found.

## 4 | DISCUSSION

Beginning with the original HH study in 1952, numerous studies have been modeled neural activity as a purely electrical phenomenon. The inclusion of the electromechanical coupling<sup>8,22</sup> (such as electrostriction<sup>21</sup> and piezoelectricity<sup>11</sup>) accompanying neural activity aims at improving the understanding of neuron-to-neuron communications, diseases, and clinical treatments.<sup>3,4,41</sup> Computational modeling is a powerful research tool to investigate and simulate these complex phenomena.

In contrast to previous studies,<sup>4,9</sup> this paper shows the advantages of a fully coupled electromechanical 3D framework to investigate the details of neural activity, combining real-time fully coupled electromechanical phenomena, a modulated threshold for spiking activation, and independent alteration of the electrical properties for each fiber in

the 3-layer nerve bundle.<sup>8,20</sup> As a development of our previous work<sup>8</sup>, here, the description of the mechanical behaviour of the nerve bundle model incorporates plasticity to represent permanent deformation of the tissue, while sharing the same approach for modelling the coupling between electrical and mechanical domains, proposed in Cinelli et al<sup>8</sup>. The Limitations section, below, addresses the limitations of this modelling approach<sup>8,20</sup> and parameters used in this paper, relevant if referring to nervous cells of specific structure and type. The use of coupled electromechanical finite element modeling for neural engineering<sup>8</sup> opens the way to a different investigation of the neuron nature itself. The use of a 3D geometry allows for a physical representation of the neuron cell and morphology in signal propagation with trauma.<sup>8,11,15,17,19,20,42</sup> Estimating the strain and stress distributions in damaged nerve fibers and bundles is a key issue both for clinical care and medical devices.<sup>1,3,4,41</sup>

Here, 2 cases of interest provide insights into the electrophysiological impairments of axonal injury due to sudden trauma-induced loading conditions. The boundary conditions in this study replicate the experiments conducted on nerve bundles and axons under both pressure<sup>2</sup> and elongation.<sup>7,15,19</sup> Additionally, the use of a 3D geometry highlights the difference in voltage and strain distributions in unmyelinated and myelinated fibers in bundles of different size.

Differences in signal transmission arise in the bundle for each fiber, depending on the fiber type. In the bundle, Fiber #3 is activated by imposing a voltage Gaussian distribution on the fiber, while the other fibers are activated based on the voltage gradient from the active fiber and total strains (elastic, equivalent thermal, and plastic strains) read at the nerve membrane.

The inclusion of plasticity shows the impact of permanent deformation on signal propagation after a mechanical load is applied. Permanent deformations occur if the strains at the nerve membrane are higher than 21 % according to Bain and Meaney,<sup>7</sup> so the reversal voltage potentials change permanently accordingly to the strain intensity. In the cases considered here, the signal read at the nerve membrane on Fiber #3 varies between ranges of voltage value lower than the action potential described by HH,<sup>24</sup> or the membrane potential is about the baseline value. This means that the distribution of voltage in the bundle is changed, and the other fibers are not activated, because the voltage read at their nerve membranes is a subthreshold stimulation, so that an action potential cannot be elicited (see Figure 5).

During compression, the neural activity is changed according to the elastic strain at the nerve membrane, where we find plastic strains of 0.5 % in unmyelinated fibers, but no plastic strains in myelinated fibers for the range of pressure levels applied. Although we chose high pressure values comparable with those found in TBI,<sup>2</sup> the applied strains do not compromise the functionality of the membrane and its ability to generate signals, even when assuming changes in ionic conductance.<sup>12</sup> Additionally, the resulting total strains at the membrane are lower than 3.5 % and 1.5 % in unmyelinated and myelinated bundles. Thus, during compression, the fiber is far from mechanical failure, thanks to the small strains generated at the membrane. Fibers and bundles appear to be stronger in compression than in elongation. A uniform compression of the bundle induces only a 1 % elongation of the bundle, leading to small changes in neural activity and lower values of plastic strains (PEs) found at the membrane.

During elongation, results show that the neural activity is more easily affected by deformations in small bundles than in larger bundles, where at 14 % of elongation a plateau indicates a new osmotic gradient across the nerve membrane (see Figure 5). As in experiments, the larger the fiber, the higher the voltage read at the membrane<sup>17,19,43</sup> and hence the higher the deformations (see Figure 7) whose plastic component is shown in Figure 6. We also find that the myelin layer constrains the mechanical deformation of the nerve membrane at the Ranvier nodes, generating a different distribution of plastic strain around the fiber. This important property of myelin preserves the functionality of the membrane by distributing the applied uniaxial strain within the bundle. It is revealed, thanks to 3D finite element modeling.

Small myelinated bundles tolerate lower plastic strain than unmyelinated bundles, as seen in previous studies.<sup>1,25,29</sup> However, smaller plastic strains are found in bigger myelinated bundles, where plastic damage occurs locally around the fiber rather than along the fiber length (see Figure 5). This could be thought of as a way to preserve good communication between neurons cells under stretch. The nervous cell reading the signals carried by a damaged myelin fiber might not consider it as a valuable source of information because of its reduced magnitude. For higher deformations, the action potential is not elicited because of the very low ionic gradient across the nerve membrane,<sup>8</sup> altering the signal propagation from cell to cell and, in turn, the communication between cells.

The assumption of instantaneous loading is a first step toward the electromechanical analysis of changes associated with TBI. Rate-dependent loadings could be included in future works. Injury pathologies in nerve fibers are also initiated and influenced by strain and strain rate, which have a significant impact on the time of neural death and pathomorphology, respectively.<sup>18</sup> Experimental studies on human axons show morphological changes of axons at different stages of dynamic stretch injury.<sup>19</sup> Axons can tolerate stretching up to twice their original length under slow loading rates (within the range of minutes<sup>30</sup>), with elastic recovery of the initial prestretched geometry.<sup>18,30</sup>

However, dynamic loading conditions with a short pulse duration (lower than  $50\text{s}^{-130}$ ) initiate undulating distortions along their entire length,<sup>18,19,30</sup> and recovery of the prestretched geometry was found to be nonuniform. Axonal regions can manifest both an elastic recovery and a delayed elastic response, ie, a gradual recovery, along the same fiber length.<sup>19</sup> For example, mechanical failure of squid giant axons was found at 25 – 30 % stretch at a strain rate of  $10\text{ s}^{-1}$ ,<sup>17</sup> while human axons, with a diameter of about 0.5 – 1  $\mu\text{m}$ , tolerate dynamic stretch injury at strains up to 65 % according to Smith et al.<sup>19</sup>

Future studies might also include viscoelastic mechanical properties for a more accurate description of the mechanical behavior of nervous fibers under loading.<sup>9</sup> An elastic isotropic plastic model, as in this paper, might not be comprehensive enough to tackle mechano-sensing properties arising during loading at different strain rates,<sup>9</sup> such as the reversible behavior of specific ionic channels after stretch, recovery, and axonal growth.<sup>9,10</sup>

Finally, as highlighted earlier, our model assumed an idealized geometry of a nerve bundle. Further works must tackle the effect of a realistic geometry of nervous cells, by considering fiber alignments in different directions and multiple fiber activation.

## 5 | CONCLUSION

We propose a fully coupled electromechanical framework for modeling the biophysical phenomena accompanying neural activity, such as electrostriction and piezoelectricity, by relying on the electrothermal analogy. This framework is a new approach in neural engineering, embracing the main findings of experimental observations. The model, built on previously published work,<sup>8,13,20</sup> incorporates the effect of plasticity to generate a fully coupled 3D simulation of ion channel leaking for nerve fibers under pressure and displacement loads. To recapitulate, this model shows the following:

- Time-shifted, signal magnitude and nerve membrane potential baseline values are found to be dependent on the total strain, voltage, and size of the fiber.
- Lower strain and lower electrophysiological changes are found in myelinated fibers than in unmyelinated fibers.
- The myelin layer redistributes the generated plastic strain within the bundle.
- Fibers and bundles are stronger under compression than elongation.
- During elongation, mechanical failure occurs at lower elongation in BBMY, than in BBUN, SBMY, and SBUN.
- Larger bundles deform more than small bundles.
- Larger bundles fail because of elastic strain, not plastic strain.
- Trauma affects small bundles more than larger bundles.
- Plastic strains are not influenced by the trauma level at the nerve membrane (as measured by AC).
- Trauma (AC) does not influence the membrane baseline voltage during compression or elongation.
- Trauma does not influence voltage and plastic strain in larger bundles.

This model can contribute to the understanding of the causes and consequences of TBI and DAI to improve diagnosis, clinical treatments, and prognosis by simulating the mechanical changes accompanying the changes in signal transmission in TAI-induced loading conditions.

### 5.1 | Limitations

This work aims at evaluating the electromechanical coupling<sup>8</sup> in a nerve bundle model, where isotropic plastic behavior is assigned to the nerve membrane, ICM, and myelin layer. This modeling approach has not been extended yet to simulate temperature variation and its implications, as has been shown to occur in nervous cells during signaling.<sup>24,44,45</sup> The inclusion of the temperature would allow for an evaluation of the changes in conduction velocity in relation to the induce damage intensity, not accounted in this paper.

To illustrate the relative effects of nerve bundle scale and the inclusion of plasticity, the electrophysiological parameters of this paper were taken from the literature used to validate the basic coupled electromechanical model.<sup>9,20,24</sup> This paper aims at highlighting the applicability of the electromechanical coupling proposed in Cinelli et al<sup>8</sup> to DAI for its relevance in clinical applications. However, future studies might take into account different material properties for

simulating alterations occurring in specific regions of the brain due to diseases,<sup>33</sup> brain aging,<sup>46</sup> human disorders,<sup>47</sup> or in other human body regions (as the human cochlea<sup>45,48</sup>).

As mentioned in section 2, this study is carried out assuming an idealized geometry of a nerve bundle to limit the complexity and computational cost arising from the use of 3D morphological images of neuronal structure.<sup>20,36</sup> Then, although the axon caliber has been shown to vary in animals<sup>28,49</sup> and in humans,<sup>31,50,51</sup> here, we have assumed fibers with diameters of about 1 to 2  $\mu\text{m}$  only, as examples of human nerve fibers. However, the human brain is made of fibers with a wider range of diameters.<sup>31,50</sup> So, the caliber of fibers considered in this paper is representative of small fibers ( $d < 0.4 \mu\text{m}$ ) only found in the human corpus callosum,<sup>31</sup> but not large fibers ( $d > 5 \mu\text{m}$ ).<sup>31</sup> Thus, future works may consider testing this modeling approach for a wider range of axon caliber to understand the distribution of functional and mechanical failure within the human brain under mechanical loading.<sup>31,45,50</sup> However, whereas the results reported in this work refer to 2 nerve bundle models only, the electromechanical coupling<sup>8</sup> in this paper builds on a previous validation, carried out in 3 different animal models with diameters varying between 0.25 and 500  $\mu\text{m}$ .<sup>20</sup>

## ACKNOWLEDGEMENTS

We gratefully acknowledge funding from the Galway University Foundation, the Biomechanics Research Centre, and the Power Electronics Research Centre, College of Engineering and Informatics at NUI Galway.

## ORCID

Ilaria Cinelli  <http://orcid.org/0000-0003-1302-1188>

Michel Destrade  <http://orcid.org/0000-0002-6266-1221>

Peter McHugh  <http://orcid.org/0000-0001-9147-3652>

Maeve Duffy  <http://orcid.org/0000-0002-1379-3279>

## REFERENCES

- Hemphill MA, Dauth S, Yu CJ, Dabiri BE, Parker KK. Traumatic brain injury and the neuronal microenvironment: a potential role for neuropathological mechanotransduction. *Neuron*. 2015;85(6):1177-1192. <https://doi.org/10.1016/j.neuron.2015.02.041>
- Hosmane S, Fournier A, Wright R, et al. Valve-based microfluidic compression platform: single axon injury and regrowth. *Lab Chip*. 2011;11(22):3888-3895. <https://doi.org/10.1039/c1lc20549h>
- Ma J, Zhang K, Wang Z, Chen G. Progress of research on diffuse axonal injury after traumatic brain injury. *Neural Plast*. 2016;2016:1-7. <https://doi.org/10.1155/2016/9746313>
- Wright RM, Ramesh KT. An axonal strain injury criterion for traumatic brain injury. *Biomech Model Mechanobiol*. 2012;11(1-2):245-260. <https://doi.org/10.1007/s10237-011-0307-1>
- Zhang YP, Cai J, Shields LBE, Liu N, Xu XM, Shields CB. Traumatic brain injury using mouse models. *Transl Stroke Res*. 2014;5(1):454-471. <https://doi.org/10.1007/s12975-014-0327-0>
- Kan EM, Ling E, Lu J. Microenvironment changes in mild traumatic brain injury. *Brain Res Bull*. 2012;87(4-5):359-372. <https://doi.org/10.1016/j.brainresbull.2012.01.007>
- Bain AC, Meaney DF. Tissue-level thresholds for axonal damage in an experimental model of central nervous system white matter injury. *J Biomech Eng*. 2000;122(6):615-622. <https://doi.org/10.1115/1.1324667>
- Cinelli I, Destrade M, Duffy M, McHugh P. Electro-mechanical response of a 3D nerve bundle model to mechanical loads leading to axonal injury. *Int J Numerical Methods Biomed Eng*. 2017a;978-981. <https://doi.org/10.1002/cnm.2942>
- Jérusalem A, García-Grajales JA, Merchán-Pérez A, Peña JM. A computational model coupling mechanics and electrophysiology in spinal cord injury. *Biomech Model Mechanobiol*. 2014;13(4):883-896. <https://doi.org/10.1007/s10237-013-0543-7>
- Shi R, Whitebone J. Conduction deficits and membrane disruption of spinal cord axons as a function of magnitude and rate of strain. *J Neurophysiol*. 2006;95(6):3384-3390. <https://doi.org/10.1152/jn.00350.2005>
- Zhang PC, Keleshian AM, Sachs F. Voltage-induced membrane movement. *Nature*. 2001;413(6854):428-432. <https://doi.org/10.1038/35096578>
- Boucher PA, Joós B, Morris CE. Coupled left-shift of Nav channels: modeling the Na<sup>+</sup>-loading and dysfunctional excitability of damaged axons. *J Comput Neurosci*. 2012;33(2):301-319. <https://doi.org/10.1007/s10827-012-0387-7>
- Cinelli I, Destrade M, Duffy M, McHugh P. Neurotrauma evaluation in a 3D electro-mechanical model of a nerve bundle. In IEEE (Ed.), *International IEEE/EMBS Conference on Neural Engineering, NER*. (pp. 513-516): 2017c. <https://ieeexplore.ieee.org/document/8008402/>

14. Mohagheghian F. (2015). Effect of geometry on propagation of action potentials in neurons; an in silico analysis. In 2015 IEEE 35th International Conference on Electronics and Nanotechnology (ELNANO) Effect (pp. 378–380). Retrieved from <http://ieeexplore.ieee.org/document/7146924/>
15. Geddes DM, Cargill RS, LaPlaca MC. Mechanical stretch to neurons results in a strain rate and magnitude-dependent increase in plasma membrane permeability. *J Neurotrauma*. 2003;20(10):1039-1049. <https://doi.org/10.1089/089771503770195885>
16. Yu N, Morris CE, Joós B, Longtin A. Spontaneous excitation patterns computed for axons with injury-like impairments of sodium channels and Na/K pumps. *PLoS Comput Biol*. 2012;8(9):e1002664. <https://doi.org/10.1371/journal.pcbi>
17. Galbraith JA, Thibault LE, Matteson DR. Mechanical and electrical responses of the squid giant axon to simple elongation. *J Biomech Eng*. 1993;115(1):13-22. <https://doi.org/10.1115/1.2895464>
18. Bar-kochba E, Scimone MT, Estrada JB, Franck C. Strain and rate-dependent neuronal injury in a 3D in vitro compression model of traumatic brain injury. *Nature Publishing Group*, (April). 2016;6:1-11. <https://doi.org/10.1038/srep30550>
19. Smith DH, Wolf JA, Lusardi TA, Lee VM, Meaney DF. High tolerance and delayed elastic response of cultured axons to dynamic stretch injury. *J Neurosci*. 1999;19(11):4263-4269. Retrieved from <http://www.jneurosci.org/content/19/11/4263.long>
20. Cinelli I, Destrade M, Duffy M, McHugh P. Electro-thermal equivalent 3D finite element model of a single neuron. *IEEE Trans Biomed Engineering*. 2017b;65(6):1373-1381. <https://doi.org/10.1109/TBME.2017.2752258>
21. Alvarez O, Latorre R. Voltage-dependent capacitance in lipid bilayers made from monolayers. *Biophys J*. 1978;21(1):1-17. [https://doi.org/10.1016/S0006-3495\(78\)85505-2](https://doi.org/10.1016/S0006-3495(78)85505-2)
22. El Hady A, Machta BB. Mechanical surface waves accompany action potential propagation. *Nat Commun*. 2015;6(6697):6697. <https://doi.org/10.1038/ncomms7697>
23. Mueller JK, Tyler WJ. A quantitative overview of biophysical forces impinging on neural function. *Phys Biol*. 2014;11(5). <https://doi.org/10.1088/1478-3975/11/5/051001>
24. Hodgkin AL, Huxley AF. A quantitative description of membrane current and its application to conduction and excitation in nerve. *J Physiol*. 1952. [https://doi.org/10.1016/S0092-8240\(05\)80004-7](https://doi.org/10.1016/S0092-8240(05)80004-7)
25. Jafari SS, Nielson M, David I, Maxwell WL. Axonal cytoskeletal changes after nondisruptive axonal injury. II. Intermediate sized axons. *J Neurotrauma*. 1998;15(11):955-966.
26. Wang HC, Ma YB. Experimental models of traumatic axonal injury. *J Clin Neurosci*. 2010;17(2):157-162. <https://doi.org/10.1016/j.jocn.2009.07.099>
27. Wang J, Hamm R, Povlishock JT. Traumatic axonal injury in the optic nerve: evidence for axonal swelling, disconnection, dieback, and reorganization. *J Neurotrauma*. 2011;28(7):1185-1198. <https://doi.org/10.1089/neu.2011.1756>
28. Perge J a, Niven JE, Mugnaini E, Balasubramanian V, Sterling P. Why do axons differ in caliber? *The J Neurosci*. 2012;32(2):626-638. <https://doi.org/10.1523/JNEUROSCI.4254-11.2012>
29. Reeves TM, Smith TL, Williamson JC, Phillips LL. Unmyelinated axons show selective rostrocaudal pathology in the corpus callosum following traumatic brain injury. *J Neuropathol Exp Neurol*. 2012;71(3):198-210. <https://doi.org/10.1097/NEN.0b013e3182482590>. Unmyelinated
30. Tang-schomer MD, Patel AR, Baas PW, Smith DH. Mechanical breaking of microtubules in axons during dynamic stretch injury underlies delayed elasticity, microtubule disassembly, and axon degeneration. *FASEB J*. 2017;24(5):1401-1410. <https://doi.org/10.1096/fj.09-142844>
31. Björnholm L, Nikkinen J, Kiviniemi V, et al. Structural properties of the human corpus callosum: multimodal assessment and sex differences. *Neuroimage*. 2017;152(February):108-118. <https://doi.org/10.1016/j.neuroimage.2017.02.056>
32. Lajtha A, Javitt D, Kantrowitz J. Handbook of neurochemistry and molecular neurobiology. Brain and spinal cord dent traumatol (N. Banik & K. R. Swapan, Eds.), *Springer Reference* (3rd Edition, Vol. 281). Springer; 2009. <https://doi.org/10.1016/j.jns.2009.03.019>
33. Demerens C, Stankoff B, Logak M, et al. Induction of myelination in the central nervous system by electrical activity. *Proc Natl Acad Sci U S A*. 1996;93(18):9887-9892. <https://doi.org/10.1073/pnas.93.18.9887>
34. Heimburg T, Blicher A, Mosgaard LD, Zecchi K. Electromechanical properties of biomembranes and nerves. *J Phys Conf Ser*. 2014;558:12018. <https://doi.org/10.1088/1742-6596/558/1/012018>
35. Mosgaard LD, Zecchi K a, Heimburg T. Mechano-capacitive properties of polarized membranes. *Soft Matter*. 2015;11(40):7899-7910. <https://doi.org/10.1039/C5SM01519G>
36. Lytton WW, Arle J, Bobashev G, et al. Multiscale modeling in the clinic: diseases of the brain and nervous system. *Brain Informatics*. 2017;4(4):219-230. <https://doi.org/10.1007/s40708-017-0067-5>
37. Plonsey R, Barr RC. *Bioelectricity: A quantitative approach* (3rd Edition, Chapter 6). Springer; 2007. <https://doi.org/10.1007/978-0-387-48865-3>
38. Einziger PD, Livshitz LM, Dolgin A, Mizrahi J. Novel cable equation model for myelinated nerve fiber. *IEEE Trans Biomed Eng*. 2005;52(10):112-115. <https://doi.org/10.1109/CNE.2003.1196769>

39. Platkiewicz J, Brette R. A threshold equation for action potential initiation. *PLoS Comput Biol*. 2010;6(7):25. <https://doi.org/10.1371/journal.pcbi.1000850>
40. Tahayori B, Meffin H, Dokos S, Burkitt AN, Grayden DB. Modeling extracellular electrical stimulation: II. Computational validation and numerical results. *J Neural Eng*. 2012;9(6):65006. <https://doi.org/10.1088/1741-2560/9/6/065006>
41. Shi R, Pryor JD. Pathological changes of isolated spinal cord axons in response to mechanical stretch. *Neuroscience*. 2002;110(4):765-777. [https://doi.org/10.1016/S0306-4522\(01\)00596-6](https://doi.org/10.1016/S0306-4522(01)00596-6)
42. Gallant PE, Galbraith JA. Axonal structure and function after axolemmal leakage in the squid giant axon. *J Neurotrauma*. 1997;14(11):811-822. <https://doi.org/10.1089/neu.1997.14.811>
43. Durand, D. M. (2000). Electric stimulation of excitable tissue. In E. J. D. Bronzino (Ed.), *The Biomedical Engineering Handbook* (Second Edition). Boca Raton: CRC Press LLC. <https://doi.org/10.1201/9781420049510>
44. Andersen SSL, Jackson AD, Heimburg T. Towards a thermodynamic theory of nerve pulse propagation. *Prog Neurobiol*. 2009;88(2):104-113. <https://doi.org/10.1016/j.pneurobio.2009.03.002>
45. Rattay, F. (2005). Functional electrical stimulation of the central nervous system: analysis of the primarily excited structures, (July), 122.
46. Ziegler G. Models of the aging brain structure and individual decline. *Front Neuroinform*. 2012;6(March):1-16. <https://doi.org/10.3389/fninf.2012.00003>
47. Bercury KK, Macklin WB. Dynamics and mechanisms of CNS myelination. *Dev Cell*. 2015;32(4):447-458. <https://doi.org/10.1016/j.devcel.2015.01.016>
48. Rattay F, Potrusil T, Wenger C, Wise AK, Glueckert R, Schrott-Fischer A. Impact of morphometry, myelination and synaptic current strength on spike conduction in human and cat spiral ganglion neurons. *PLoS One*. 2013;8(11):e79256. <https://doi.org/10.1371/journal.pone.0079256>
49. Wang SS-H, Shultz JR, Burish MJ, et al. Functional trade-offs in white matter axonal scaling. *J Neurosci*. 2008;28(15):4047-4056. <https://doi.org/10.1523/JNEUROSCI.5559-05.2008>
50. Liewald D, Miller R, Logothetis N, Wagner HJ, Schüz A. Distribution of axon diameters in cortical white matter: an electron-microscopic study on three human brains and a macaque. *Biol Cybern*. 2014;108(5):541-557. <https://doi.org/10.1007/s00422-014-0626-2>
51. Rattay F, Potrusil T, Wise AK, et al. Impact of morphometry, myelination and synaptic current strength on spike conduction in human and cat spiral ganglion. Impact of morphometry, myelination and synaptic current strength on spike conduction in human and cat spiral ganglion neurons, (November). *PLoS One*. 2013;8(11):e79256. <https://doi.org/10.1371/journal.pone.0079256>

**How to cite this article:** Cinelli I, Destrade M, McHugh P, Duffy M. Effects of nerve bundle geometry on neurotrauma evaluation. *Int J Numer Meth Biomed Engng*. 2018;e3118. <https://doi.org/10.1002/cnm.3118>